Twist Without Tangle: Flutter Suppression of Thin-Walled Wing-Engine Systems via Curvilinear Fiber Path Tailoring and Cross-Section Optimization

Nima Kakhsaz Malayeri[1]
[1] Department of Aerospace Engineering, Amirkabir University of Technology, Tehran, Iran
E-Mail: Nima.Kakhsaz.m@gmail.com

Abstract

Flutter is traditionally delayed by modifying either a structure's geometry or its stiffness distribution. Here, we show that allowing both to evolve simultaneously can unlock a fundamentally different route to aeroelastic stability. We concurrently optimize the cross-sectional geometry and fiber paths of a composite thin-walled wing–engine system to maximize flutter onset. The wing structure is modeled using Classical Laminated Plate Theory, while unsteady aerodynamic loads are represented by a Mach-number-corrected Wagner state-space formulation. The engine is modeled as a lumped mass with rotational inertia, follower thrust, and its associated gyroscopic reaction. The wing cross-section is parameterized as an arbitrary smooth closed curve, while fiber orientation is independently varied throughout the wing structure. A continuous penalty formulation prevents pinching, self-intersection, and excessive curvature during optimization. The optimization employs a modified Parallelized Complex Method (PCM) originally proposed by Namani Koureh et al. (2026) for fiber path optimization, reformulated here to accommodate variable cross-sectional geometry. The optimized designs achieve an approximately 42% increase in flutter speed relative to fiber-only optimization. Notably, this improvement does not result from suppressing the conventional flapwise flutter mechanism. Instead, simultaneous geometry–fiber tailoring fundamentally alters the aeroelastic instability pathway, with flutter onset becoming governed by a chordwise mode. These results demonstrate that concurrent optimization of structural geometry and fiber paths can redirect aeroelastic instability toward an alternative mode in thin-walled wing-engine systems.

Keywords: Flutter Optimization, Shape Optimization, Curvilinear Fiber Path Tailoring, Self-intersection Barrier

1. Introduction

Composite structures have traditionally relied on straight or constant-angle plies; however, advances in manufacturing techniques allowed fiber paths to vary spatially within a laminate, introducing a broader design space for tailoring local stiffness (Gurdal and Olmedo 1993; Honda and Narita 2011). This variable-stiffness (VS) concept has subsequently been extended to T-shaped panels (Chagraoui and Soula 2024), buckling of composite wing boxes (Huang et al. 2024), biconvex thin-walled sections (Haddadpour and Zamani 2012), and integrated aeroelastic tailoring (Bordogna et al. 2020), with studies reporting improved performance and stability (Kalanchiam and Chinnasamy 2012). Thin-walled beam theory, developed extensively by Librescu and Song (2006), provides the foundation for many of the aeroelastic models used in these investigations. For wing-mounted engines, stability analyses have progressively incorporated engine inertia, thrust (Farsadi et al. 2019), and gyroscopic effects (Namani Koureh et al. 2026), demonstrating that these couplings can substantially modify the aeroelastic response (Mardanpour et al. 2013). The incorporation of VS laminates into such engine-coupled systems has further revealed the potential of fiber-path tailoring to influence aeroelastic stability (Asadi et al. 2021).

The influence of thrust on flutter predates the introduction of fiber-path tailoring as a design variable. Feldt and Herrmann (1974) investigated the flutter of a cantilevered wing subjected to a follower thrust force exerted by a lumped tip mass, while Hodges et al. (2002) subsequently established a direct relationship between thrust magnitude, the bending-to-torsion stiffness ratio, and the onset of instability. More recently, flutter-speed maximization through fiber-path tailoring has been pursued using Genetic Algorithms (Gu et al. 2012; Asadi et al. 2021), Particle Swarm Optimization (Yu et al. 2022), and deep-learning-based approaches for shape optimization (Chen et al. 2026). However, population-based methods can become increasingly computationally expensive as the fiber parametrization and corresponding design space grow in complexity. To address this challenge, Namani Koureh et al. (2026) proposed a Parallelized Complex Method (PCM) for optimizing a bivariate distribution of fiber angles throughout the wing while retaining a fixed rectangular cross-section.

In contrast, cross-sectional shape optimization has been investigated across a broad range of engineering applications. Optimized boundaries have been considered in pontoon design (Lu et al. 2025), aircraft wing shape and topology optimization (Høghøj et al. 2023), airfoil optimization (Dussauge et al. 2023; Chen et al. 2026), bodies in Navier–Stokes flow (Garcke et al. 2018), acoustic scatterers (Hiptmair et al. 2018), and full-aircraft aerodynamic shape optimization (Tfaily et al. 2024).

Several geometric representations have been developed to parametrize shape optimization problems, including splines and Bézier curves (Piegl and Tiller 1997; Pekerman et al. 2008), Fourier series (Zahn and Roskies 1972; Deng et al. 2022), and level-set methods (van Dijk et al. 2013). A recurring challenge in these applications is the emergence of self-intersecting boundaries during optimization. Once a boundary crosses itself, any finite-element mesh constructed from the resulting geometry may become invalid. This issue has also been encountered in reinforcement-learning-based airfoil optimization, where unrestricted movement of control points can produce tangled geometries. Subsequent approaches have mitigated this problem by restricting the design variables to thickness and camber modifications rather than permitting unrestricted search (Dussauge et al. 2023). Within these representations, three broad strategies have been adopted; to prevent by construction (Zelickman and Guest 2025; van Dijk et al. 2013; Norato 2018; Lee and Sheikh 2026) or resolve self-intersection by removing it (Pekerman et al. 2008) or penalizing it (Walker 2016; Wu et al. 2019; Yu et al. 2021; Sassen et al. 2024; Paul et al. 2021).

Despite these advances, the integration of a continuous geometric penalty with an exact algebraic self-intersection criterion, rather than heuristic proximity-based penalties such as those proposed by Yu et al. (2021), has not yet been established for aeroelastic shape optimization.

The integration of freely optimized cross-sectional geometry with flutter-speed maximization remains comparatively unexplored. Mardanpour et al. (2019) modified wing cross-sections to smooth the internal stress flow and reported a corresponding increase in flutter speed, while Moshtaghzadeh et al. (2022) employed an evolutionary search to optimize flying-wing cross-sectional geometries for the same objective. However, neither study integrates cross-sectional optimization with bidirectional fiber-path tailoring and wing-mounted engine dynamics, nor does either explicitly address self-intersection of the evolving cross-section through a discrete methodology that avoids constraining the design space. This gap motivates a unified aeroelastic optimization that couples geometric and stiffness tailoring.

Addressing both gaps, we extend and modified the PCM approach of Namani Koureh et al. (2026) by replacing its fixed rectangular cross-section with an arbitrary Fourier-parameterized boundary and jointly optimizing the cross-sectional geometry and bidirectional fiber paths to maximize the flutter speed of a wing–engine system. In addition to enforcing closedness and boundedness, geometric admissibility is ensured through the algebraic self-intersection barrier introduced by

Kakhsaz Malayeri (2026), which is incorporated directly into the flutter-speed objective rather than imposed through an a posteriori feasibility check. The formulation further suppresses cusp formation and excessive curvature, maintaining physically and numerically admissible cross-sections throughout the optimization. This unified approach allows structural stiffness tailoring and cross-sectional geometry to evolve concurrently, expanding the aeroelastic design space beyond approaches in which fiber architecture is optimized independently on a fixed cross-section. More broadly, the proposed approach is not restricted to flutter optimization and can be extended to a wide range of multidisciplinary optimization problems involving fluid–structure interaction (FSI) systems.

2. Governing Equations

Fig. 1 depicts a widely adopted model for Thin-Walled Wing–Engine (TWWE) system, consisting of:(1) a load-bearing structure modeled as a single-cell, cantilevered thin-walled composite beam with a bivariate fiber-orientation distribution; (2) an engine that introduces follower thrust, gyroscopic reaction torque, and rotational inertia; and (3) unsteady aerodynamic loading acting on the wing (Namani Koureh et al. 2026).

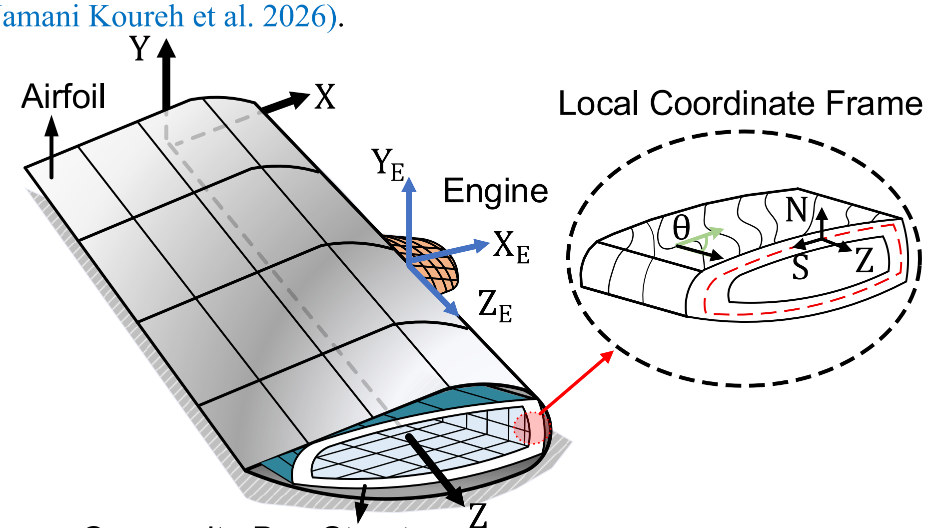

Fig. 1 Schematic of TWWE system, global (XYZ), local (NSZ), and engine ($X_E Y_E Z_E$) coordinate systems, mid-line curve of cross section (dash), and fiber angle (θ)

Under the following modeling assumptions: (1) small-displacement kinematics incorporating transverse shear deformation, wall-thickness effects, and cross-sectional warping; (2) constitutive behavior described by Classical Laminate Theory (CLT); (3) unsteady aerodynamic loading represented using Wagner's state-space approximation within lifting-line theory; and (4) the engine represented as a lumped mass. Namani Koureh et al. (2026) derive the equations of motion of the thin-walled wing–engine (TWWE) system using a Ritz expansion, yielding:

$$\frac{\mathrm{d}\boldsymbol{\Theta}}{\mathrm{d}t} = -\begin{bmatrix} \mathrm{M}_{\mathrm{FSI}}^{-1} & 0 & 0 \\ 0 & \mathrm{I} & 0 \\ 0 & 0 & \mathrm{I} \end{bmatrix} \begin{bmatrix} \mathrm{C}_{\mathrm{FSI}} & \mathrm{K}_{\mathrm{FSI}} & -\mathrm{F}_{\mathrm{w}} \\ -\mathrm{I} & 0 & 0 \\ -\mathrm{C}_{\mathrm{w}} & -\mathrm{K}_{\mathrm{w}} & \mathrm{D}_{\Lambda} \end{bmatrix} \begin{bmatrix} \dot{\boldsymbol{\eta}} \\ \boldsymbol{\eta} \\ \boldsymbol{\Lambda} \end{bmatrix} = \mathrm{D}\boldsymbol{\Theta} \tag{1}$$

where

$$\begin{aligned} \mathrm{M}_{\mathrm{FSI}} &= \mathrm{M}_{\mathrm{s}} + \mathrm{M}_{\mathrm{E}} - \mathrm{M}_{\mathrm{F}} \\ \mathrm{K}_{\mathrm{FSI}} &= \mathrm{K}_{\mathrm{s}} - \mathrm{K}_{\mathrm{E}} - \mathrm{K}_{\mathrm{F}} \\ \mathrm{C}_{\mathrm{FSI}} &= -\mathrm{C}_{\mathrm{F}} - \mathrm{G}_{\mathrm{E}} \end{aligned}$$

Here, M, K, and C are the mass, stiffness, and damping matrices, with subscripts F, s, E, and w indicating the fluid, structural, engine, and aerodynamic lag-state contributions. G_{E} represents the damping associated with the engine reaction torque. The vectors $\boldsymbol{\eta}$ and $\boldsymbol{\Lambda}$ contain the structural generalized coordinates and aerodynamic lag states, respectively; $\mathrm{F_w}$ is the corresponding Wagner-induced aerodynamic force, and D_{Λ} is the lag-state system matrix.

In this formulation of TWWE, Namani Koureh et al. (2026) derived the aerodynamic loading under the assumption of incompressible flow and evaluate the flutter speed at relatively high subsonic Mach numbers ($\mathrm{Ma} \approx 0.45$), where the validity of this assumption becomes increasingly restrictive. Further improvements in flutter performance through geometric optimization is suspected to shift the operating regime toward even higher Mach numbers, making compressibility effects increasingly important. Accordingly, Appendix A gives the correction factors required to incorporate compressibility effects into Equation (1).

2.1 Problem Statement

The dynamic stability of the TWWE system is governed by the eigenvalues of the system matrix D, which are functions of both the fiber paths θ and the cross-sectional geometry $\boldsymbol{\tau}$. Consequently, these two design variables provide independent yet intrinsically coupled means of modifying the aeroelastic stability characteristics of the system.

At zero freestream velocity ($u_\infty = 0$), the system in (1) is marginally stable. As u_∞ increases, the system becomes unstable once an eigenvalue of D crosses into the right-half of the complex plane, defining the critical flutter speed u_∞^{c}. Optimization problem (2) therefore seeks the cross-sectional geometry and fiber paths that maximize u_∞^{c}:

$$(\boldsymbol{\tau}^*, \theta^*) = \underset{\boldsymbol{\tau},\theta}{\operatorname{argmax}}\, u_\infty^{\mathrm{c}}(\boldsymbol{\tau}, \theta) \tag{2}$$

This optimization is subject to six geometric constraints: (C1) bounded fiber curvature; (C2) closure of the cross-sectional midline; (C3) confinement of the midline within a prescribed bounding box; (C4) bounded curvature of the cross-sectional midline; (C5) absence of self-intersections of the midline; and (C6) regularity of the midline curve. To solve the optimization problem in Equation (2) subject to constraints (C1)–(C6), the cross-sectional geometry $\boldsymbol{\tau}$ and fiber-angle distribution θ are parameterized using the conventions introduced by Kakhsaz Malayeri (2026) and Honda et al. (2013), respectively.

2.1.1 Cross-Section Shape

The cross-sectional midline of the TWWE is represented by

$$\boldsymbol{\tau}(t) = [x(t) \quad y(t)]^{\mathrm{T}} \quad , \quad t \in [0,1]$$

and parametrized using a truncated Fourier series:

$$\boldsymbol{\tau}(t) = \begin{bmatrix} x(t) \\ y(t) \end{bmatrix} = \sum_{n=0}^{N} \begin{bmatrix} a_{x_n} \\ a_{y_n} \end{bmatrix} \cos 2\pi n t + \begin{bmatrix} b_{x_n} \\ b_{y_n} \end{bmatrix} \sin 2\pi n t \qquad t \in [0\ 1] \tag{3}$$

The corresponding design vector is defined as

$$\boldsymbol{x}_\tau = \left[a_{x_1}, \cdots, a_{x_N}, b_{x_1}, \cdots, b_{x_N}, a_{y_1}, \cdots, b_{y_N}\right]$$

Because the structural formulation requires an arc-length parametrization of the cross-sectional midline, the normalized parameter t is converted to arc-length through

$$g(t) = \int_0^t \sqrt{\dot{x}^2(t) + \dot{y}^2(t)}\, dt \quad , \quad \boldsymbol{\tau}_s(s) = \boldsymbol{\tau}\big(g^{-1}(s)\big)$$

Here, $\boldsymbol{\tau}_s(s)$ denotes the cross-sectional midline expressed in terms of its arc-length coordinate s, which is required for the evaluation of the system matrices D.

2.1.2 Fiber Angle Distribution

The fiber-angle distribution $\theta(s,z)$ is parametrized following the methodology introduced by Honda et al. (2013):

$$\tan\theta(s,z) = \left(\frac{-\partial f}{\partial s}\right)\left(\frac{\partial f}{\partial z}\right)^{-1} \quad , \quad f(s,z) = \sum_{i=0}^{p}\sum_{j=0}^{p} a_{ij}\left(\frac{z}{L}\right)^{i}\left(\frac{s}{\beta}\right)^{j} \tag{4}$$

The corresponding design vector is

$$\boldsymbol{x}_\theta = \left[a_{pp}, \cdots, 1, a_{01}\right]$$

Here, L and β represent the wing span and the total length of the cross-sectional midline, respectively. To implement the fiber-path parametrization (4), the structural domain is discretized into small tiles along the circumferential and spanwise directions, with dimensions Δs and Δz. Within each tile, the fibers are oriented tangent to the contour line of $f(s,z)$ that passes through the tile center, and maintaining uniform fiber volume fraction among tiles. Fig. 2 illustrates the resulting domain discretization and fiber-layout procedure.

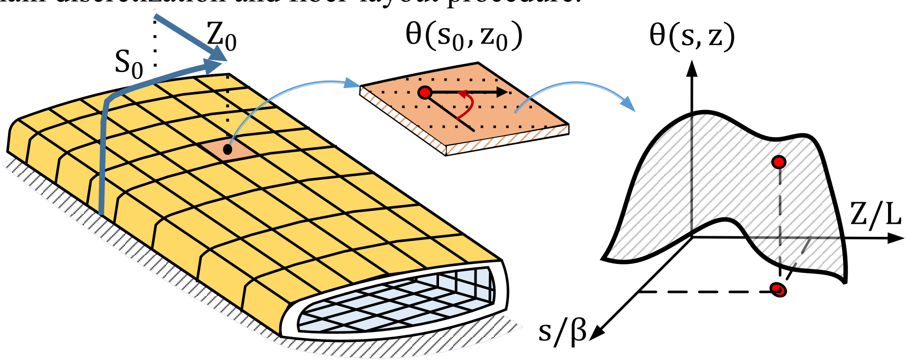

Fig. 2 Illustrations of discretization and sampling of fiber angles throughout the wing

2.1.3 Discussion on Optimization Conditions

Six constraints must be enforced in the optimization problem (2). Constraint (C1) limits the maximum curvature of the fiber paths. Following Namani Koureh et al. (2026), this constraint is imposed indirectly by restricting the fiber-angle design vector $\boldsymbol{x}_\theta$ to a bounded hyper-rectangular domain:

$$\boldsymbol{x}_\theta \in [-\mathrm{B}_\theta \; \mathrm{B}_\theta]^{d} = R_\theta \quad , \quad d_\theta = (p+1)(p+2)/2 - 2 \tag{5}$$

Here, d_θ denotes the dimensionality of the fiber-path design space.

Constraint (C2) requires closure of the cross-sectional midline ($\boldsymbol{\tau}(0) = \boldsymbol{\tau}(1)$) which is inherently satisfied by the Fourier representation in Equation (3). To ensure that the cross-section remains bounded within a prescribed rectangular region (C3), the triangle inequality gives:

$$\begin{bmatrix} |x(t)| \\ |y(t)| \end{bmatrix} \leq N\sqrt{2} \begin{bmatrix} \max\limits_{n}\{a_{x_n}, b_{x_n}\} \\ \max\limits_{n}\{a_{y_n}, b_{y_n}\} \end{bmatrix} \leq \begin{bmatrix} B_{x_\tau} \\ B_{y_\tau} \end{bmatrix} \tag{6}$$

Accordingly, the Fourier coefficients are restricted to a hyper-rectangular design domain $\mathcal{R}_\tau \subset \mathbb{R}^{d_\tau}$, with $d_\tau = 4N$.

Constraints (C4)–(C6), concerning bounded midline curvature, absence of self-intersection, and curve regularity, are strongly coupled and cannot be imposed directly through simple bounds on the Fourier coefficients. In particular, excessive local curvature can promote self-intersection, while regularity is required to avoid cusps and to ensure the existence of a valid arc-length parametrization ($\parallel \boldsymbol{\tau}'(t) \parallel > 0$). These constraints could be imposed as hard geometric constraints; however, doing so would require every candidate set of Fourier coefficients generated during the optimization to undergo a feasibility check before the flutter-speed objective is evaluated.

Repeated rejection of infeasible candidates can substantially increase the computational cost, reduce the efficiency of the search, or stall optimization process.

To avoid this check-and-reject procedure, geometric feasibility is incorporated directly into the objective through the penalty function φ introduced by Kakhsaz Malayeri (2026). The penalty is constructed to decrease continuously as the cross-sectional midline approaches configurations exhibiting self-intersection, cusp formation, or excessive curvature. Thus, infeasible configurations are progressively penalized as they are approached, rather than being rejected only after being generated. Including φ barrier in optimization problem (2) yields:

$$(\boldsymbol{x}_{\tau}^{*}, \boldsymbol{x}_{\theta}^{*}) = \underset{\boldsymbol{x}_{\tau}, \boldsymbol{x}_{\theta}}{\operatorname{argmin}} \left(-\frac{u_{\infty}^{\mathrm{c}}(\boldsymbol{x}_{\tau}, \boldsymbol{x}_{\theta})}{u_{\infty}^{\mathrm{ref}}} + \lambda \frac{\varphi^{\mathrm{ref}}}{\varphi(\boldsymbol{x}_{\tau})} \right) \quad \text{subject to} \quad \mathrm{C1}, \mathrm{C3} \tag{7}$$

Here, λ is a weighting factor, while $u_{\infty}^{\mathrm{ref}}$ and φ^{ref} are reference values used to normalize the flutter-speed and geometric-penalty contributions, respectively. The barrier function is constructed such that $\varphi \to 0$ as the midline curve approaches a configuration exhibiting self-intersection, a cusp, or unbounded curvature (Kakhsaz Malayeri 2026).

2.2 Optimization Methodology

The optimization problem (7) is solved using the Parallelized Complex Method (PCM) proposed by Namani Koureh et al. (2026). PCM employs a parallelized divide-and-conquer strategy in which the design space is partitioned into smaller cells. Within each cell, an initial Complex is constructed from randomly generated seed points, after which the Complex evolves toward an optimum while progressively contracting around the converged solution. A challenge in applying PCM to the problem (7) is the generation of sufficiently diverse initial Fourier-represented cross-sectional geometries that are simultaneously free of self-intersection, regular, and suitable for initializing the Complexes. Randomly generated Fourier coefficients can readily produce geometrically invalid curves, making the construction of an adequate initial population non-trivial. Therefore, to generate adequate initial seeds, the cross-sectional design space $\boldsymbol{x}_{\tau}$ is first partitioned into m_{τ} cells, denoted by $\mathcal{C}_{\tau}^{(i)}$, $1 \le i \le m_{\tau}$. Within each cell, n_c candidate geometries are generated randomly. Because these candidates are generated without explicit geometric constraints, they may exhibit cusps, self-intersections, excessive curvature, or other forms of irregularity and therefore cannot be used directly as initials.

We address this issue by augmenting the PCM method of Namani Koureh et al. (2026) with a pre-processing step. Rather than outright rejecting invalid initial seeds — drawn both from random sampling and a set of handpicked basic geometric shapes such as circles, ovals, and polygons — in search of new ones, the resulting cross-section curves are steered toward admissible configurations by minimizing the barrier function for these curves within their original cell ($\mathcal{C}_{\tau}^{(i)}$):

$$\left(\boldsymbol{x}_{\tau_j}^{\mathrm{f}}\right)^{(i)} = \underset{\boldsymbol{x}_{\tau}}{\operatorname{argmax}}\, \varphi(\boldsymbol{x}_{\tau}) \qquad \begin{array}{c} \boldsymbol{x}_{\tau} \in \mathcal{C}_{\tau}^{(i)} \\ 1 \le j \le n_c \end{array} \tag{8}$$

This auxiliary optimization is performed for a fixed and limited number of Pattern Search iterations. The iteration count is deliberately restricted because excessive refinement can cause initially distinct candidates within the same cell to converge toward a common local optimum, thereby diminishing the diversity of the resulting seed population. After the prescribed number of Pattern Search iterations, candidates satisfying $\varphi\left(\boldsymbol{x}_{\tau_j}^{f}\right) \ge \varphi^{\mathrm{th}}$ are retained as feasible cross-sectional seeds. These seeds are subsequently paired with fiber-angle designs to initialize the PCM optimization. Specifically, the fiber-design space $\boldsymbol{x}_{\theta}$ is partitioned into m_{θ} cells, $\mathcal{C}_{\theta}^{(i)}$, $1 \le k \le m_{\theta}$, and each feasible cross-sectional seed is paired with a fiber-angle design. The resulting paired designs constitute the initial seed population for the PCM solution of optimization problem (7). To ensure that each Complex contains the same number of vertex (same Complex size d) the total number of initial candidates n_c is selected such that $n_c \gg d$. Fig. 3 illustrates this process.

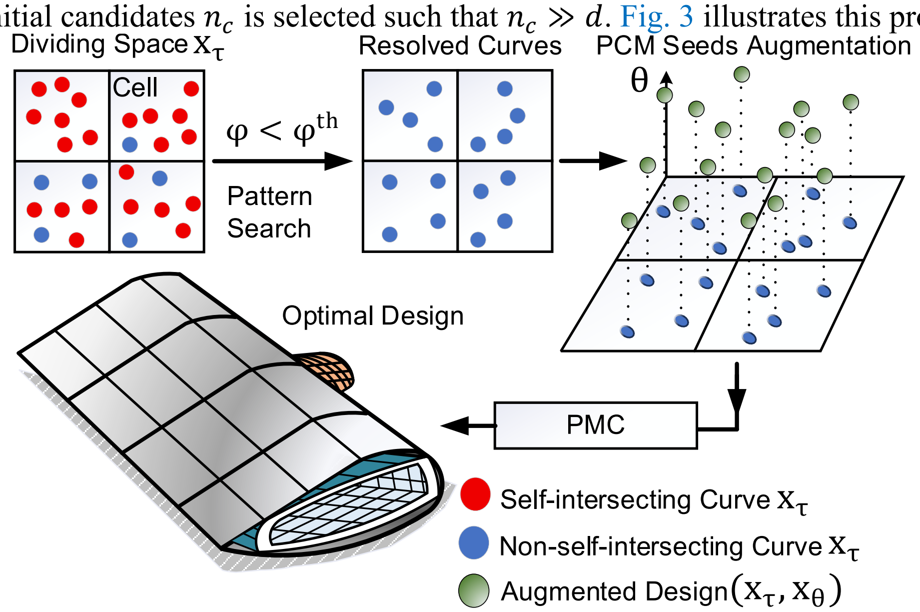

Fig. 3 Schematics of the Optimization process

By incorporating this pre-processing step, the proposed strategy ensures that each Complex is initialized with a diverse set of geometrically admissible designs while maintaining broad coverage of the cross-sectional design space.

3. Numerical Results

The case-study thin-walled wing–engine system investigated by Namani Koureh et al. (2026) and Farsadi et al. (2019) is shown in Fig. 4, with the corresponding geometric and material properties summarized in Table 1. Using this case study, we present our numerical results for the optimization problem (7).

Table 1 TWWE system parameters for optimization

Subsystem	Parameter	Value	Units
Structure	(h, L)	(0.03,14)	m
	(E_1, E_2, E_3)	(206.75, 5.17, 5.17)	Gpa
	(G_{12}, G_{13}, G_{23})	(3.1, 3.1, 2.55)	GPa
	$(\nu_{12}, \nu_{13}, \nu_{23})$	0.25	-
	ρ_s	1528.15	Kg.m^{-3}
Aerodynamic	ρ	1.224	Kg.m^{-3}
	$(2b, ba_0)$	(1.6, -0.16)	m
Engine	m_E	275	Kg
	p_E	83.18	KN
	$\boldsymbol{L}$	6480	Kg.m^2. s^{-1}
	$(\kappa_x, k_y, \kappa_\phi, x_E, z_E)$	(0.6, 0.3, 0.3, 0.2,10.5)	m

Here, h denotes the wall thickness, and L is the wing length. The symbols E_i and G_{ij} represent the Young's and shear moduli, respectively, while ν_{ij} denotes the Poisson's ratios, ρ_s and ρ represent the material and air densities, respectively. The parameter b represents the wing chord length, and

ba_0 is the distance between the geometric center of the wing structure and the airfoil center. For the engine, m_E denotes the engine mass, p_E is the engine thrust, and $\boldsymbol{L}$ is the engine reaction torque constant. The parameter κ represents the engine radius of gyration, while x_E and z_E denote the engine offsets.

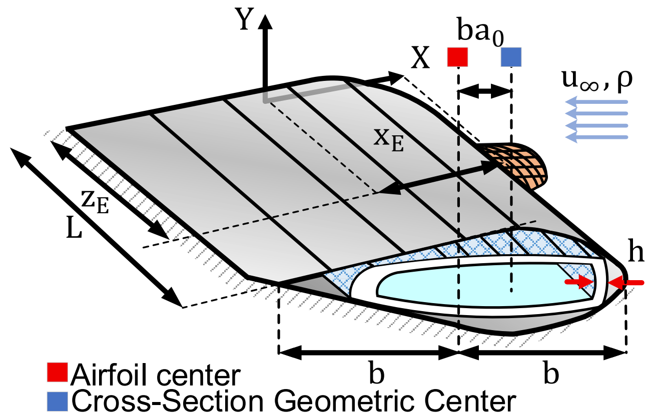

Fig. 4 Schematic of TWWE system with its geometric parameters

We present our numerical results in three stages. We first validate our formulation against the results of Namani Koureh et al. (2026) and Farsadi et al. (2019), who both restrict their analysis to a rectangular cross-section. We then extend these studies to arbitrary cross-sections by solving the optimization problem (7), and finally we post-process the resulting optimal designs.

3.1 Validation

To validate our formulation against the results reported by Namani Koureh et al. (2026) and Farsadi et al. (2019), we first consider their respective optimal fiber paths within our geometry-free formulation. Both studies assume a rectangular cross-section and report optimal fiber distributions for their respective designs. To incorporate these designs into our formulation, we approximate the rectangular cross-sectional geometry of these studies using $N = 40$ Fourier harmonics and prescribe the corresponding fiber paths reported in the two studies. For Namani Koureh et al. (2026), the reported fiber distribution is specified by

$$x_\theta = [-1.35 \quad -6.40 \quad -6.80 \quad 3.89 \quad 0.24 \quad 1.72 \quad -9.14 \quad 1 \quad -2.67]$$

whereas for Farsadi et al. (2019), it is given by

$$\theta(z) = -1.21z + 0.48.$$

Using these fiber angles together with the reconstructed rectangular cross-sections, we calculate the corresponding flutter speeds (incompressible) and compare them with the reported values in Table 2. For this analysis, we discretize the s and z coordinates using 200 and 68 nodes, respectively, and retain eleven Ritz terms in the formulation of matrix D in Equation (1). This choice of discretization and Ritz terms ensures convergence of the computed flutter speed, as demonstrated by Namani Koureh et al. (2026).

Table 2 Flutter analysis validation

Case	Flutter Speed (m/s)	
	Reference	Present
Namani Koureh et al. (2026)	176.84	179.29
Farsadi et al. (2019)	127	128.13

The results in Table 2 show good agreement with the reported values, validating our extension of the geometry-free formulation for flutter-speed prediction.

3.2 Optimization

To ensure a fair comparison between our results and those reported by Namani Koureh et al. (2026), we enforce the same total midline curve length (β) by introducing a second penalty term into the objective function:

$$(\boldsymbol{x}_{\tau}^{*}, \boldsymbol{x}_{\theta}^{*}) = \underset{\boldsymbol{x}_{\tau},\boldsymbol{x}_{\theta}}{\operatorname{argmin}} \left(-\frac{u_{\infty}^{\mathrm{c}}(\boldsymbol{x}_{\tau}, \boldsymbol{x}_{\theta})}{u_{\infty}^{\mathrm{ref}}} + \lambda \frac{\varphi^{\mathrm{ref}}}{\varphi(\boldsymbol{x}_{\tau})} + 100 \left(\frac{\beta(\boldsymbol{x}_{\tau})}{1.714} - 1 \right)^{2} \right) \tag{9}$$

The additional penalty term drives β toward the reference value of 1.714, thereby ensuring that the resulting wing designs have the same total weight as the reference design.

Table 3 Solver and Optimizer parameters

Solver	Parameter	Value
Flutter	$(\Delta s, \Delta z)$	(68,201)
	n	7
	p	3
	N	2-6
Bounds	$(\mathrm{B}_{x_\tau}, \mathrm{B}_{y_\tau})$	(0.75,0.1)
	B_{θ}	10
	ε_{C}	0.001
	ε_{B}	0.125
Optimizer	$(\lambda, u_{\infty}^{\mathrm{ref}}, \varphi^{\mathrm{ref}})$	(0.1,100,2.5)
	(m_{θ}, m_{τ})	(96,36)
	d	30
	Optimization Runs	20

Here, n, ε_{C}, and ε_{B} denote the number of Ritz terms, the convergence threshold for the PCM, and the convergence threshold for the bisection-based root-finding procedure used in the flutter-speed solver, respectively, following Namani Koureh et al. (2026). The optimization is performed on a 96-core AMD CPU operating at 3.8 GHz. The resulting optimal designs are presented in Table 4 and Fig. 5 and while linearly accounting for compressibility effects (Appendix A).

Table 4 Optimization results for $2 \leq N \leq 6$, $\beta = 1.714 \pm 0.7\%$

Case	Flutter speed (m/s)
$N = 2$	68.98
$N = 3$	129.44
$N = 4$	176.32
$N = 5$	215.05
$N = 6$	218.85

For $N = 5$ case, the corresponding optimal design variables are:

$$\begin{aligned}
\boldsymbol{x}_{\theta}^{*}(1{:}9) &= [9.81 \quad -8.96 \quad -8.41 \quad 9.11 \quad -0.91 \quad -6.56 \quad -8.41 \quad 1 \quad 9.70] \\
\boldsymbol{x}_{\tau}^{*}(1{:}5) &= 10^{-1}[2.948 \quad 0.5813 \quad 0.1884 \quad 0.1015 \quad 0.1093] \\
\boldsymbol{x}_{\tau}^{*}(6{:}10) &= 10^{-1}[-3.0549 \quad -0.5820 \quad -0.2069 \quad 0.2250 \quad 0.1048] \\
\boldsymbol{x}_{\tau}^{*}(11{:}15) &= 10^{-2}[-5.8791 \quad 1.0633 \quad 0.3530 \quad 0.5967 \quad 0.1053] \\
\boldsymbol{x}_{\tau}^{*}(16{:}20) &= 10^{-2}[-5.8883 \quad 1.0602 \quad 0.3641 \quad -0.1822 \quad -0.099]
\end{aligned} \tag{10}$$

Furthermore, as shown in Equation (10), the higher harmonics exhibit progressively lower amplitudes, indicating that additional harmonics beyond $N \geq 6$ are unlikely to meaningfully improve the predicted flutter speed while also risking unwanted oscillatory features in the cross-sectional geometry.

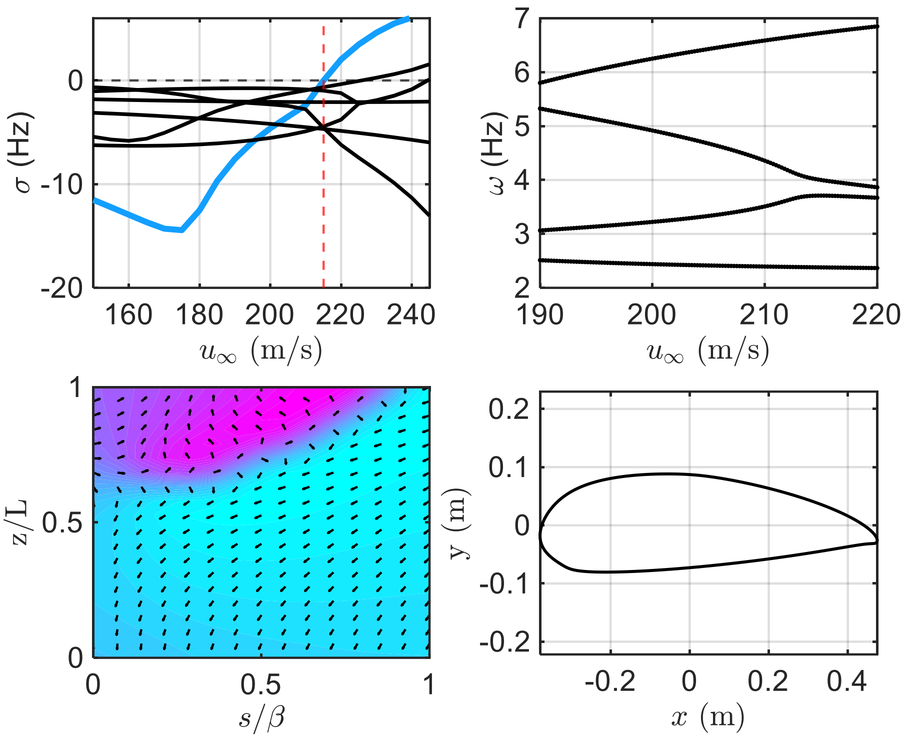

Fig. 5 Optimization results for $N = 5$, (A) real part of eigenvalues of matrix D with respect to free-stream speed (u_∞), (B) imaginary part of eigenvalues of matrix D with respect to free-stream speed (u_∞), (C) fiber paths, (D) optimized geometry

Solution (10) achieves $\beta = 1.7180$ and $u_\infty^c = 215.05$ m/s (Ma $= 0.63$) closely matching the reference value of 1.714 and enabling a fair comparison with Namani Koureh et al. (2026) in the next section.

3.3 Post-Processing

We first consider the effect of two corrections in Equation (1) — chordwise migration of the elastic axis ($a(z)$) across the wingspan and the Mach number correction to the aerodynamic loading as illustrated in Fig. 6.

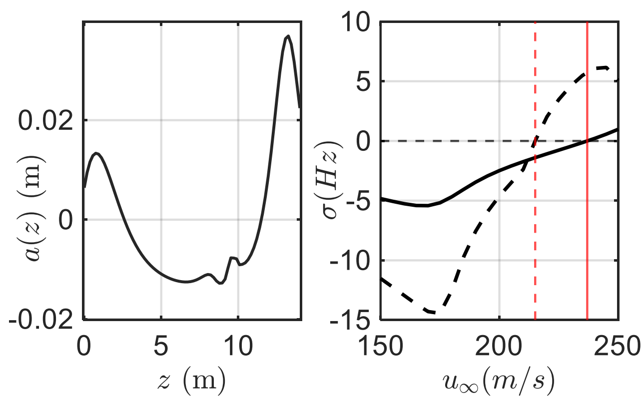

Fig. 6 Correction Factors, (left) Elastic axis deviation due to geometric and ply angle asymmetry, (right) effect of Mach number on flutter speed — solid line indicating compressible flow

As shown in Fig. 6, the elastic axis (e.a.) of the wing migrates by approximately 6 cm across the wingspan. Neglecting this migration increases the predicted flutter speed to $u_\infty^c = 219.77$m/s, corresponding to an overprediction of approximately 2%. This difference is relatively small and expected for the present design. However, for a more adverse configuration with highly asymmetric ply angles, this effect can reach up to 12%.

Neglecting compressibility in the aerodynamic model further increases the predicted flutter speed to $u_\infty^c = 237$m/s, corresponding to a 10% overprediction. When both elastic-axis migration and compressibility are neglected, the predicted flutter speed increases further to $u_\infty^c = 247$m/s, resulting in a 15% overprediction. These results indicate that the two modeling simplifications interact and can amplify the overall error when neglected simultaneously.

To further investigate the effects of geometry and ply-angle optimization, we consider six cases, summarized in Table 5: **(**Basic**)** a TWWE system with a constant zero ply angle and simple oval geometry with $\beta = 1.714$; **(**Geometry**)** the TWWE system with only the optimized geometry $\boldsymbol{x}_\tau^*$ applied and zero ply angle; **(**Ply**)** the same oval geometry with only the optimized ply-angle variables $\boldsymbol{x}_\theta^*$ applied; **(**Optimized**)** the fully optimized design with both $\boldsymbol{x}_\tau^*$ and $\boldsymbol{x}_\theta^*$ applied using the values from (10); **(**Uni-ply**)** the optimized geometry $\boldsymbol{x}_\tau^*$ with a constant non-zero ply angle selected to maximize the flutter speed, $\theta = 78°$; and **(**Reference**)** the reference design reported by Namani Koureh et al. (2026).

Table 5 Flutter speed comparison, all cases have $\beta = 1.714 \pm 0.3\%$

Case	u_∞^c (m/s)	Improvement	Correction	
			Ma	e.a
Basic	21.85	-	✓	✓
Geometry	111.69	5.11x	✓	✓
Ply	105.96	4.84x	✓	✓
Optimized	215.05	9.84x	✓	✓
Uni-ply	118.16	5.40x	✓	✓
Reference	176.84	8.09x	✗	✓
Reference	151.27	6.92x	✓	✓

Attained results in Table 5 demonstrate that simultaneously optimizing the cross-sectional geometry and ply angles can substantially increase the flutter speed. To gain further insight into the physical mechanism responsible for this improvement, Fig. 7 shows the bending-to-torsion ratio of the critical eigenvalue at the wing tip ($z = L$) as a function of free-stream speed for the optimal configuration obtained from Equation (10).

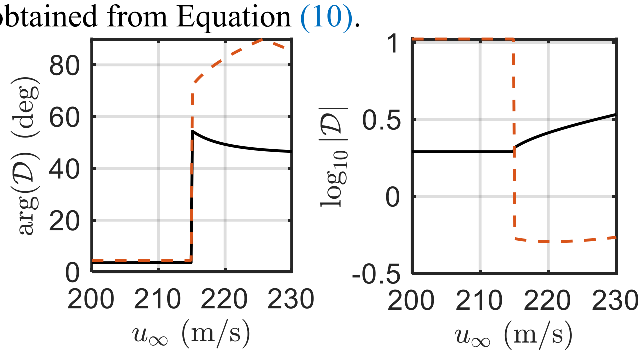

Fig. 7 Bending to torsion ratio, chordwise (solid) and flap-wise (dash)

As indicated by the kink in Fig. 7 at $u_\infty^c = 215.05$ m/s flutter happens. Around this speed we extract the unstable eigenvalue and its corresponding eigenvector in order to calculate the flapwise (v) and chordwise (u) bending to torsion (ϕ) ratios $\mathcal{D}_v = v(L)/\phi(L)$ and $\mathcal{D}_u = u(L)/\phi(L)$, respectively. Below the flutter speed, both ratios remain close to a 0°phase angle, with $\mathcal{D}_u$ exhibiting a substantially higher amplitude than $\mathcal{D}_v$. At the instability crossing, the phase of $\mathcal{D}_u$

shifts abruptly to approximately $75^\circ - 85^\circ$, indicating a near-quadrature phase relationship between chordwise bending and torsion and, indicating a possible strong aerodynamic energy transfer to the structure. In contrast, $\mathcal{D}_v$ reaches only approximately $50^\circ - 55^\circ$. These results indicate that the flutter mechanism in the optimal design given by (10) is primarily driven by chordwise bending rather than the flapwise-bending mechanism typically associated with flutter. To investigate the origin of this behavior further, we report the span-averaged stiffnesses across the various designs in Table 6.

Table 6 Spanwise average of stiffness matrix

Coupling stiffness	Baseline	Geometry	Ply	Optimized	Amplification
Flapwise	6.35	1.84×10^5	2.76×10^6	6.27×10^6	2.27×
Chordwise	0	0	4.40×10^6	1.11×10^7	2.53×

These results are consistent with the findings in Fig. 7. The span-averaged stiffness matrix reveals two distinct coupling pathways. Path A, corresponding to flapwise bending–torsion coupling, can arise for any cross-sectional geometry, including a symmetric geometry with a uniform ply angle, through an offset between the elastic and reference axes. Path B, corresponding to chordwise bending–torsion coupling, in contrast, requires non-uniform fiber tailoring; for a uniform ply angle, this coupling vanishes algebraically regardless of geometric asymmetry. Once activated by fiber tailoring, Path B is further amplified by geometric asymmetry, increasing by approximately ~2.5×, compared with approximately ~2.3×, for Path A. The dynamic results in Fig. 7 provide direct evidence of this structural bias: at the flutter boundary, Path B, rather than the conventionally dominant Path A, governs the instability. We therefore attribute the improved flutter speed of the combined design to a shift in the governing coupling mechanism, enabled by fiber tailoring and reinforced by geometric optimization and existing engine mounting offset of x_E, rather than to suppression of the conventional flapwise flutter mode.

3.3.1 Optimization Complexity

The optimization problem in Equation (9) comprises three terms: the first represents the flutter-speed objective, the second is the barrier function φ, which penalizes self-intersecting geometries, and the third enforces a constant total mass across designs. Because the barrier function alone cannot guarantee a valid initial design, we precede the PCM proposed by Namani Koureh et al. (2026) with a preprocessing stage. In this stage, we apply a limited pattern-search algorithm to randomly generated Fourier curves to identify non-self-intersecting designs, which we then use to initialize the PCM. The barrier function φ plays a critical role in preventing self-intersecting designs during the optimization. This is important because self-intersections can corrupt or prevent the flutter-speed calculation, causing the optimization to terminate prematurely or, more problematically, yielding invalid designs that may nevertheless be favored by the optimizer and lead to false convergence. Over more than 50 million function evaluations during the optimization, the optimizer never crossed into the self-intersecting region of the design space while exploring it. We independently verified this result without relying on the barrier function output (φ); instead, we used the exact self-intersection solver provided in the code supplied by Kakhsaz Malayeri (2026). Table 7 further reports the average evaluation time associated with each of the three terms in the objective function and total run-time of the optimization.

Table 7 run-time of the Optimization

Function	u_∞^c	φ	β
Average call time (ms)	258	33	0.01
Total run-time	53.21 hours		

4. Conclusion

We maximized the flutter speed of a composite thin-walled wing with a wing-mounted engine by optimizing cross-sectional geometry and fiber orientation together. The cross-section is represented as an arbitrary closed curve using a truncated Fourier series, and fiber angles are parameterized with an established bivariate polynomial scheme (Namani Koureh 2026), letting geometry and fiber architecture vary freely. A continuous algebraic penalty built directly into the optimization objective enforces geometric admissibility — blocking self-intersection, cusp formation, and excessive curvature without a separate feasibility check at every iteration (Kakhsaz Malayeri 2026). We solved the resulting problem with a Parallelized Complex Method (PCM), preceded by a preprocessing step that generates diverse, non-self-intersecting initial cross-sections. Compressibility and elastic-axis migration are also captured, keeping the aeroelastic model accurate at the higher flutter speeds the optimization reaches.

For the representative wing–engine system, joint optimization of geometry and fiber orientation raised the flutter speed considerably over the untailored baseline, by roughly a factor of two over fiber-path tailoring alone on an oval cross-section, and by 42% against Namani Koureh et al. (2026) — without adding structural weight. Across more than 57 million function evaluations, the penalty never let the optimizer select a self-intersecting cross-section, confirming that geometric admissibility held throughout the search. Additionally, we showed that the gain does not come from strengthening the classical flapwise bending–torsion coupling. Instead, non-uniform fiber tailoring activates a chordwise bending–torsion coupling pathway absent in uniform-ply designs, and geometric asymmetry amplifies it further. This shift in the dominant coupling mechanism explains the large flutter-speed increase achieved by optimizing geometry and fiber orientation together.

We expect this PCM–barrier approach to extend beyond aeroelasticity to broader fluid–structure interaction problems involving geometry changes, follower forces, added-mass effects, and strong fluid–structure coupling.

Declarations

Funding: No funding was received for conducting this study.

Conflict of interest: The authors declare that they have no conflict of interest.

Ethics approval: This article does not contain any studies with human participants or animals performed by any of the authors.

Consent to participate: Not applicable.

Consent for publication: Not applicable.

Data availability: Data and materials supporting the findings of this study are available from the corresponding author upon reasonable request.

Replication of results: Codes are uploaded as supplementary material.

Author Contribution: Solo Author.

LLM Usage: Limited to Language editing, Grammar checking, catching mathematical notation errors, extraction of DOIs

References

Asadi D, Farsadi T, Kayran A (2021) Flutter optimization of a wing–engine system with passive and active control approaches. AIAA J 59(4):1422–1440. doi.org/10.2514/1.J059568

Bakhtiari-Nejad F, Modaress-Aval AH, Dowell EH, Shahverdi H (2017) Linear and nonlinear aeroelastic analysis of a high aspect ratio wing using Wagner's unsteady aerodynamic model. In: Proceedings of the ASME 2017 International Design Engineering Technical Conferences and

Computers and Information in Engineering Conference (IDETC/CIE), Cleveland, USA, Paper DETC2017-67289. ASME. doi.org/10.1115/DETC2017-67289
Bordogna MT, Lancelot P, Bettebghor D, De Breuker R (2020) Static and dynamic aeroelastic tailoring with composite blending and manoeuvre load alleviation. Struct Multidiscip Optim 61:2193–2216. doi.org/10.1007/s00158-019-02446-w
Chagraoui H, Soula M (2024) Maximum buckling load design and post-buckling compressive failure of curved grid sub-stiffened composite panels. Eur J Mech A Solids 107:105381. doi.org/10.1016/j.euromechsol.2024.105381
Chen Y, Li J, Song C, et al (2026) Aerodynamic shape optimization with effective deep-learning-based geometric filtering: from a cylinder to a wing. Struct Multidiscip Optim 69:25. doi.org/10.1007/s00158-025-04235-0
Deng F, Xue C, Qin N (2022) Parameterizing airfoil shape using aerodynamic performance parameters. AIAA J 60(7):4399–4412. doi.org/10.2514/1.J061464
Dussauge TP, Sung WJ, Pinon Fischer OJ, Mavris DN (2023) A reinforcement learning approach to airfoil shape optimization. Sci Rep 13:9753. doi.org/10.1038/s41598-023-36560-z
Farsadi T, Asadi D, Kurtaran H (2019) Flutter improvement of a thin-walled wing-engine system by applying curvilinear fiber path. Aerosp Sci Technol 93:105353. doi.org/10.1016/j.ast.2019.105353
Feldt WT, Herrmann G (1974) Bending-torsional flutter of a cantilevered wing containing a tip mass and subjected to a transverse follower force. J Franklin Inst 297(6):467–478. doi.org/10.1016/0016-0032(74)90123-9
Garcke H, Hinze M, Kahle C, Lam KF (2018) A phase field approach to shape optimization in Navier–Stokes flow with integral state constraints. Adv Comput Math 44:1345–1383. doi.org/10.1007/s10444-018-9586-8
Gu Y, Zhang X, Yang Z (2012) Robust flutter analysis based on genetic algorithm. Sci China Technol Sci 55:2474–2481. doi.org/10.1007/s11431-012-4944-0
Gurdal Z, Olmedo R (1993) In-plane response of laminates with spatially varying fiber orientations: variable stiffness concept. AIAA J 31(4):751–758. doi.org/10.2514/3.11613
Haddadpour H, Zamani Z (2012) Curvilinear fiber optimization tools for aeroelastic design of composite wings. J Fluids Struct 33:180–190. doi.org/10.1016/j.jfluidstructs.2012.05.008
Hiptmair R, Scarabosio L, Schillings C, Schwab C (2018) Large deformation shape uncertainty quantification in acoustic scattering. Adv Comput Math 44:1475–1518. doi.org/10.1007/s10444-018-9594-8
Hodges DH, Patil MJ, Chae S (2002) Effect of thrust on bending-torsion flutter of wings. J Aircraft 39(2):371–376. doi.org/10.2514/2.2937
Høghøj LC, Conlan-Smith C, Sigmund O, Andreasen CS (2023) Simultaneous shape and topology optimization of wings. Struct Multidiscip Optim 66:116. doi.org/10.1007/s00158-023-03569-x
Honda S, Igarashi T, Narita Y (2013) Multi-objective optimization of curvilinear fiber shapes for laminated composite plates by using NSGA-II. Compos Part B Eng 45(1):1071–1078. doi.org/10.1016/j.compositesb.2012.07.056
Honda S, Narita Y (2011) Vibration design of laminated fibrous composite plates with local anisotropy induced by short fibers and curvilinear fibers. Compos Struct 93(2):902–910. doi.org/10.1016/j.compstruct.2010.07.003
Huang Y, Wang Z, Chen P (2024) Buckling optimization of variable stiffness composite wing boxes with manufacturing defects. Struct Multidiscip Optim 67:109. doi.org/10.1007/s00158-024-03809-8

Kakhsaz Malayeri N (2026) Rooting Out Self-Intersection: An Algebraic Shape-Optimization Barrier. Optimization Online optimization-online.org/?p=36614

Kalanchiam M, Chinnasamy M (2012) Advantages of composite materials in aircraft structures. Int J Aerosp Mech Eng 6(11):2428–2432. doi.org/10.5281/zenodo.1060473

Lee S, Sheikh HM (2026) Airfoil optimization using Design-by-Morphing with minimized design-space dimensionality. J Comput Des Eng 13(1):108–124. doi.org/10.1093/jcde/qwaf124

Leishman JG, Nguyen KQ (1990) State-space representation of unsteady airfoil behavior. AIAA J 28:836–844. doi.org/10.2514/3.25127

Librescu L, Song O (2006) The equations of motion of open/closed cross-section beams. In: Thin-Walled Composite Beams: Theory and Application. Springer, pp 63–84. doi.org/10.1007/1-4020-4203-5_3

Lu C, Xu L, Guo A, et al (2025) Shape optimization of floating bridge pontoons with mooring constraints under wave actions. Struct Multidiscip Optim 68:53. doi.org/10.1007/s00158-025-03985-1

Mardanpour P, Hodges DH, Neuhart R, Graybeal N (2013) Engine placement effect on nonlinear trim and stability of flying wing aircraft. J Aircraft 50(6):1716–1725. doi.org/10.2514/1.C031955

Mardanpour P, Izadpanahi E, Rastkar S, Lorente S, Bejan A (2019) Constructal design of aircraft: flow of stresses and aeroelastic stability. AIAA J 57(10):4393–4405. doi.org/10.2514/1.J057183

Moshtaghzadeh M, Izadpanahi E, Bejan A, Mardanpour P (2022) Evolutionary aeroelastic design of flying-wing cross section. AIAA J 60(2):913–924. doi.org/10.2514/1.J060410

Namani Koureh Koureh S, Shahverdi H, Kakhsaz Malayeri N, Amoozgar M (2026) Parallelized complex method for multidisciplinary optimization of aeroelastic performance in thin-walled wing–engine system using bidirectional curvilinear fiber pathing. Struct Multidiscip Optim 69:157. doi.org/10.1007/s00158-026-04311-z

Norato JA (2018) Topology optimization with supershapes. Struct Multidiscip Optim 58:415–434. doi.org/10.1007/s00158-018-2034-z

Paul EJ, Landreman M, Antonsen T (2021) Gradient-based optimization of 3D MHD equilibria. J Plasma Phys 87(2):905870215. doi.org/10.1017/S0022377821000283

Pekerman D, Elber G, Kim MS (2008) Self-intersection detection and elimination in freeform curves and surfaces. Comput Aided Des 40(2):150–159. doi.org/10.1016/j.cad.2007.10.004

Piegl L, Tiller W (1997) The NURBS Book, 2nd edn. Springer, Berlin. doi.org/10.1007/978-3-642-59223-2

Sassen J, Schumacher H, Rumpf M, Crane K (2024) Repulsive shells. ACM Trans Graph 43(4):Article 140. doi.org/10.1145/3658174

Tfaily A, Diouane Y, Bartoli N, et al (2024) Bayesian optimization with hidden constraints for aircraft design. Struct Multidiscip Optim 67:123. doi.org/10.1007/s00158-024-03833-8

Van Dijk NP, Maute K, Langelaar M, Van Keulen F (2013) Level-set methods for structural topology optimization: a review. Struct Multidiscip Optim 48(3):437–472. doi.org/10.1007/s00158-013-0912-y

Walker SW (2016) Shape optimization of self-avoiding curves. J Comput Phys 311:275–298. doi.org/10.1016/j.jcp.2016.02.011

Wu Z, Jiang W, Luo H, Cheng L (2019) A novel self-intersection penalty term for statistical body shape models and its applications in 3D pose estimation. Appl Sci 9(3):400. doi.org/10.3390/app9030400

Yu C, Schumacher H, Crane K (2021) Repulsive curves. ACM Trans Graph 40(2):Article 10. doi.org/10.1145/3439429
Yu C, Li Y, Chen Q, He J, Zhao L (2022) An advanced particle swarm optimization algorithm and its application to search flutter critical velocity of bridges. Adv Struct Eng 25(11):2271–2283. doi.org/10.1177/13694332221092670
Zahn CT, Roskies RS (1972) Fourier descriptors for plane closed curves. IEEE Trans Comput C-21(3):269–281. doi.org/10.1109/TC.1972.5008949
Zelickman Y, Guest JK (2025) Introducing a general polygonal primitive for feature mapping-based topology optimization. Struct Multidiscip Optim 68:99. doi.org/10.1007/s00158-025-04034-7

Appendix A – Formulation of Compressible Aerodynamic Loading.

Wagner's state-space formulation for lift (L) and pitching moment (M) about the airfoil's elastic axis are given by (Leishman and Nguyen 1990; Bakhtiari-Nejad et al. 2017):

$$
\begin{gathered}
L(z,t) = -\rho\pi b^2\left(-\ddot{v}_0 + u_\infty\dot{\phi} - ba\ddot{\phi}\right) + \\
\frac{\pi\rho b u_\infty}{\sqrt{1-\mathrm{Ma}^2}}\left(-\dot{v}_0 + u_\infty\phi + b\left(\frac{1}{2}-a\right)\dot{\phi}\right) + \frac{2\pi\rho b u_\infty}{\sqrt{1-\mathrm{Ma}^2}}\left(\gamma_{1_w}\lambda_1 + \gamma_{2_w}\lambda_2\right) \\
M(z,t) = -\rho\pi b^3\left(-a\ddot{v}_0 - u_\infty\left(\frac{1}{2}-a\right)\dot{\phi} - b\left(a^2+\frac{1}{8}\right)\ddot{\phi}\right) + \\
\frac{\pi\rho u_\infty b^2}{\sqrt{1-\mathrm{Ma}^2}}\left(a+\frac{1}{2}\right)\left(-\dot{v}_0 + u_\infty\phi + b\left(\frac{1}{2}-a\right)\dot{\phi}\right) + \frac{2\pi\rho u_\infty b^2}{\sqrt{1-\mathrm{Ma}^2}}\left(\frac{1}{2}+a\right)\left(\gamma_{1_w}\lambda_1 + \gamma_{2_w}\lambda_2\right)
\end{gathered}
\tag{A.1}
$$

Where ϕ denotes torsion, v_0 represents bending, ρ is the air density, u_∞ the free-stream speed, b the half-chord of the airfoil, and a the offset between the elastic axis, Ma is Mach number and a the airfoil mid-chord, normalized by b.

The coefficients γ_{i_w} are given by $\gamma_{i_w} = (1-\mathrm{Ma}^2)\alpha_i\beta_i u_\infty/b$, and the aerodynamic lag states $\lambda_i(i=1,2)$ satisfy the conditions:

$$
\dot{\lambda}_i(z,t) + \beta_i(1-\mathrm{Ma}^2)\frac{u_\infty}{b}\lambda_i(z,t) = -\dot{v}_0 + u_\infty\phi + b\left(\frac{1}{2}-a\right)\dot{\phi} \quad , \quad i=1,2 \tag{A.2}
$$

where the coefficients are $(\alpha_1,\alpha_2) = (0.165\,,0.335)$ and $(\beta_1,\beta_2) = (0.0445\,,0.35)$.